

Article

# A Self-Tuned Method for Impedance-Matching of Planar-Loop Resonators in Conformable Wearables

Sen Bing , Khengdauliu Chawang and J.-C. Chiao \* 

Electrical and Computer Engineering, Southern Methodist University, Dallas, TX 75205, USA

\* Correspondence: Jchiao@smu.edu

**Abstract:** Loop structure has been used as a single resonator and in meta-materials. Variations from the loop structures such as split-ring resonators have been utilized as sensing elements in integrated devices for wearable applications or in array configurations for free-space resonance. Previously, impedance formula and equivalent circuit models have been developed for a single loop made of a conductor wire with a negligible wire diameter in the free space. Despite the features of being planar and small, however, the quality factors of single-loop resonators or antennas have not been sufficiently high to use them efficiently for sensing or power transfer. To investigate the limitation, we first experimentally examined the formula and equivalent circuits for a single loop made of planar metal sheets, along with finite element simulations. The loop performance factor was varied to validate the formula and equivalent circuits. Then a tuning element was utilized in the planar loop to improve resonance by providing distributed impedance-matching to the loop. The proposed tuning method was demonstrated with simulations and measurements. A new equivalent circuit model for the tuned loop resonator was established. Quality factors at resonance show significant improvement and the tuning can be done for a specific resonance order without changing the loop radius. It was also shown that the tuning method provided more robust performance for the resonator. The tuning mechanism is suitable for miniature planar device architectures in sensing applications, particularly for implants and wearables that have constraints in dimensions and form factors. The equivalent circuit model can also be applied for meta-materials in arrayed configurations.

**Keywords:** loop resonator; tuning; impedance-matching; quality factor



**Citation:** Bing, S.; Chawang, K.; Chiao, J.-C. A Self-Tuned Method for Impedance-Matching of Planar-Loop Resonators in Conformable Wearables. *Electronics* **2022**, *11*, 2784. <https://doi.org/10.3390/electronics11172784>

Academic Editor: José Santa

Received: 14 August 2022

Accepted: 2 September 2022

Published: 4 September 2022

**Publisher's Note:** MDPI stays neutral with regard to jurisdictional claims in published maps and institutional affiliations.



**Copyright:** © 2022 by the authors. Licensee MDPI, Basel, Switzerland. This article is an open access article distributed under the terms and conditions of the Creative Commons Attribution (CC BY) license (<https://creativecommons.org/licenses/by/4.0/>).

## 1. Introduction

Small-loop resonators have been used for sensing, signal transduction, and power transfer applications since they are relatively easy to make in micro- and nano-scales, integrate with electronics, and be applied with meta-materials [1–6]. In the microwave frequency ranges, small-loop resonators are compliant with planar device structures, and thus, are considered for integration in microfluidic and physical biosensors, wireless power transfer, and near-field communications for implants and wearables [7–14]. Variations of the loop resonator such as the split-ring configurations provide signal isolation between the outer ring, serving for signal coupling, and the inner split ring, providing standing-wave resonance according to its length. Thus, it is easier to manage the designs without worrying about the impedance mismatch when connecting the resonator to other parts of the circuit. For example, a non-invasive continuous glucose monitoring system based on microwave split-ring resonators was proposed [9]. Gizem et al. [10] fabricated a split-ring resonator-based sensor on a flexible substrate for glaucoma monitoring on eyes. Choi et al. [11,12] demonstrated a design for blood glucose monitoring using a 3-D resonator cavity, containing two ring resonators, placed on the chest. The sensing ring is closer to the skin and responds to dielectric characteristic changes in blood with resonant frequency shifts. Another ring serves as the reference resonator for temperature calibration.

However, such split rings are typically tuned outside the ring structures and the fundamental mode of resonance is determined by the inner ring. Thus, the quality factor is

limited. In this work, we aim to examine and improve the impedance-matching issue of a single loop without implementing the split-ring structure. The metal loop usually has poor resonance performance due to its impedance mismatch, as predicted by analytical theories on loops made of metal wire [15–17]. Similarly, the issue occurs for planar metal loops in which metal thickness is much smaller than the width. Typically, the inductance and capacitance of the planar ring are obtained by finite-element simulation or empirically at the resonate frequencies. Additional matching circuits for the loop using lumped capacitors and resistors may increase insertion losses. Matching circuits also bring non-negligible frequency shifts and make the loop resonator larger or bulkier.

In this work, a new self-tuned method for impedance-matching of the loop resonator was analytically and experimentally investigated. We conducted a series of comparisons among equivalent circuits, finite-element simulations, and measurements to verify McKinley's analysis [17], which was based on wire loops, for the proposed planar loop resonators. The limitations of the theory were also studied. In Section 3, our proposed tuning element for loop resonators was introduced and demonstrated with similar equivalent circuits and verified by simulations. Measurements were conducted and compared to the results from finite-element simulations and equivalent circuits to verify our theory. The discrepancy between measurements and simulations due to the connectors were discussed and verified. The demonstration showed significant improvement on the resonance quality factors and tunability for different dimensions without increasing the footprints of resonators. The principles and equivalent circuits developed could be applied in general applications.

## 2. Limitations of Loop Resonators

According to the ring resonator theory, a metal loop will resonate when a circumference is an integer number of the wavelength, as  $2\pi b = n\lambda_0$  where  $b$  is the radius of the ring and  $\lambda_0$  is the wavelength in the medium, for a metal loop width and thickness much smaller than its radius. However, the exact relationship does not hold. Many found discrepancies in the resonant frequencies and resonance quality factors. The effect is often considered as contributions from parasitic reactance and resistance. Common approaches use estimated and/or measured inductance  $L$  and capacitance  $C$  from the metal loop to conclude the resonant frequency as  $1/\sqrt{LC}$ . The method does not provide information about the quality factor since the resistance of the metal loop needs to be evaluated at the resonant frequency, and it becomes more difficult as the operating frequency increases.

To address the problem, Storer analytically studied the impedance of a metal loop without substrate by applying an infinite Fourier series for current distributions [15]. The examination of the loop impedance reveals the exact resonant and anti-resonant frequencies along with their resonance performance. Later, McKinley et al. [17] expanded with the finite integration technique (FIT) theory on the impedances at resonance conditions and established an equivalent circuit, shown in Figure 1. In McKinley's analysis, the loop resonance performance is decided by a unitless measure  $\Omega = 2\ln(2\pi b/a)$  where  $a$  is the radius of the solid metal wire, and  $b$  is the radius of the wire ring. In this work, the loops become planar, thus, we redefined  $\Omega$  as  $U = 2\ln(2\pi b/a)$  where  $a$  is defined as the half width of the metal line because of the planar nature of the device. We would also prefer to avoid the confusion between the  $\Omega$  factor in [17] and the impedance unit  $Ohm$ . For a fixed radius  $b$ , a higher  $U$  led to a better resonance, as predicted by the formula [17]. The resistance-inductance-capacitance ( $R$ - $L$ - $C$ ) values were determined by the impedances evaluated at the resonance points. The classic impedance functions developed by Storer [15] and Wu [16] could be transformed into the equivalent circuit in Figure 1.

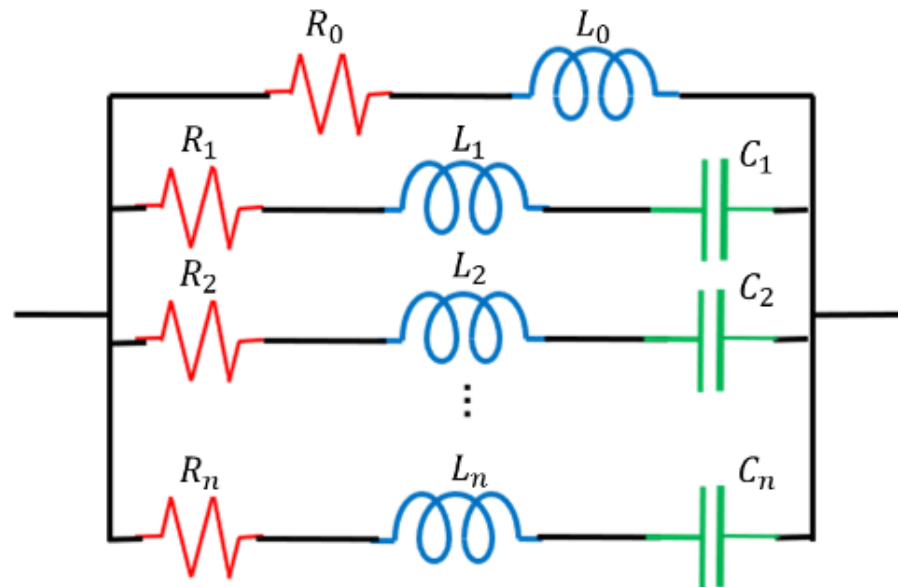


**Figure 1.** The equivalent circuit for loop resonator [17].

The resonant frequency is determined at the point where the reactance of the loop becomes zero while the reactance changes from negative to positive (capacitive to inductive reactance), as compared to the anti-resonance, where the reactance changes from inductive to capacitive with the real part of impedance reaching a peak value. At the resonance point, the current travels and becomes a standing wave along the loop. At the anti-resonance point, the current directions become opposite at certain points in the loop, so little current is available to form a standing wave along the ring. By the analytical equations in [15,17], the resonant and anti-resonant frequencies, as well as their respective impedances, can be obtained. The spectral characteristics of the impedance determine the quality factor of resonance.

For our analysis in this work,  $b = 20.9$  mm was chosen and fixed in the equations in [17] to approximate a resonant frequency within the industrial, scientific, and medical (ISM) band around 2.4 GHz. First, we verified the equivalent circuit model by conducting finite-element simulations and measurements with the  $U$  values from 8 to 11.

### 2.1. Simulations

The dimensions for simulations, shown in Figure 2a, have a radius  $b$  of 20.9 mm and a metal width of  $2a = 4.8$  mm, 2.88 mm, 1.76 mm, and 1.06 mm, for  $U = 8, 9, 10,$  and  $11$ , respectively. The thickness of the copper sheet with a conductivity of  $5.8 \times 10^7$  S/m is 0.0345 mm. A 50- $\Omega$  lumped port connects the gap for excitation. Reflection coefficients are extracted at 1001 frequency sampling points from 0 to 10 GHz. Figure 3 shows the comparison of simulation results for each  $U$  value. Resonances occur roughly at similar frequency points among each configuration but not exactly the same. This is due to that the reactive part of the loop impedance does not pass the zero value at the desired frequencies, yet rather just be close to it. This phenomenon is more prominent as  $U$  decreases and at higher orders of resonance. For the 50- $\Omega$  port, the minimum point of  $|s_{11}| = |(R + jX - 50)/(R + jX + 50)|$ —where  $R$  and  $X$  are the real and imaginary parts of the loop impedance, and both are functions of frequency—does not only depend on  $R$  but also  $X$ . Thus, the resonance points deviate from the frequencies where the reactance has been expected to be zero. All of their fundamental resonant frequencies are still within the ISM band at 2.49, 2.45, 2.42, and 2.38 GHz. The variation is 110 MHz. The loop with a higher  $U$  has a sharper spectral shape at expected resonant points, matching well with the theory [17].

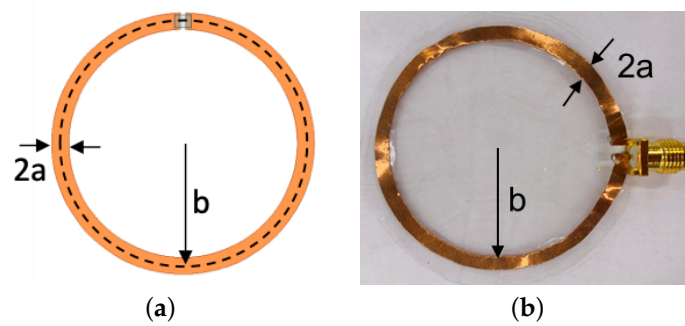


**Figure 2.** (a) Loop resonator configuration.  $b$  is the radius;  $2a$  is the planar loop width. (b) Photo of a loop resonator for measurement in which  $U = 9$ ,  $b = 20.9$  mm, and  $a = 1.44$  mm. The metal thickness is 0.0345 mm.

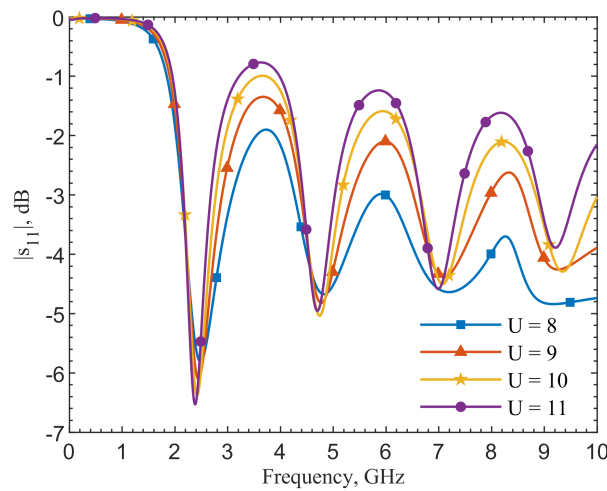


**Figure 3.** Comparison of simulations for loop resonators with  $U$  from 8 to 11.

2.2. Measurements

Loop resonators with the same configurations and made of copper sheets, shown in Figure 2b, were used in measurements. A 50-Ω SMA adaptor connected the resonator to a vector network analyzer (Keysight PNA N5227B). Figure 4 shows the measurement results for each  $U$ . Same to simulations, a higher  $U$  leads to a better resonance. The obvious discrepancies in magnitudes and spectral shapes of  $|s_{11}|$  are due to the SMA adaptor. The effects of the adaptor were investigated and verified later in the Section 5.

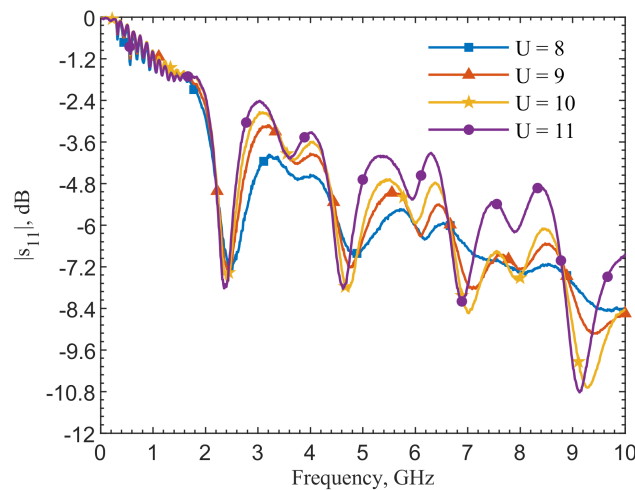


**Figure 4.** Comparison of measurements for loop resonators with  $U$  from 8 to 11.

### 2.3. Comparison of Each $U$

The calculations from the resonant equivalent circuit models, finite-element simulations, and measurement results are compared for each  $U$  value in Figure 5. The equivalent circuit considers five branches ( $Z_0, Z_1, Z_2, Z_3, Z_4$ ) for the first four resonances within 10 GHz.

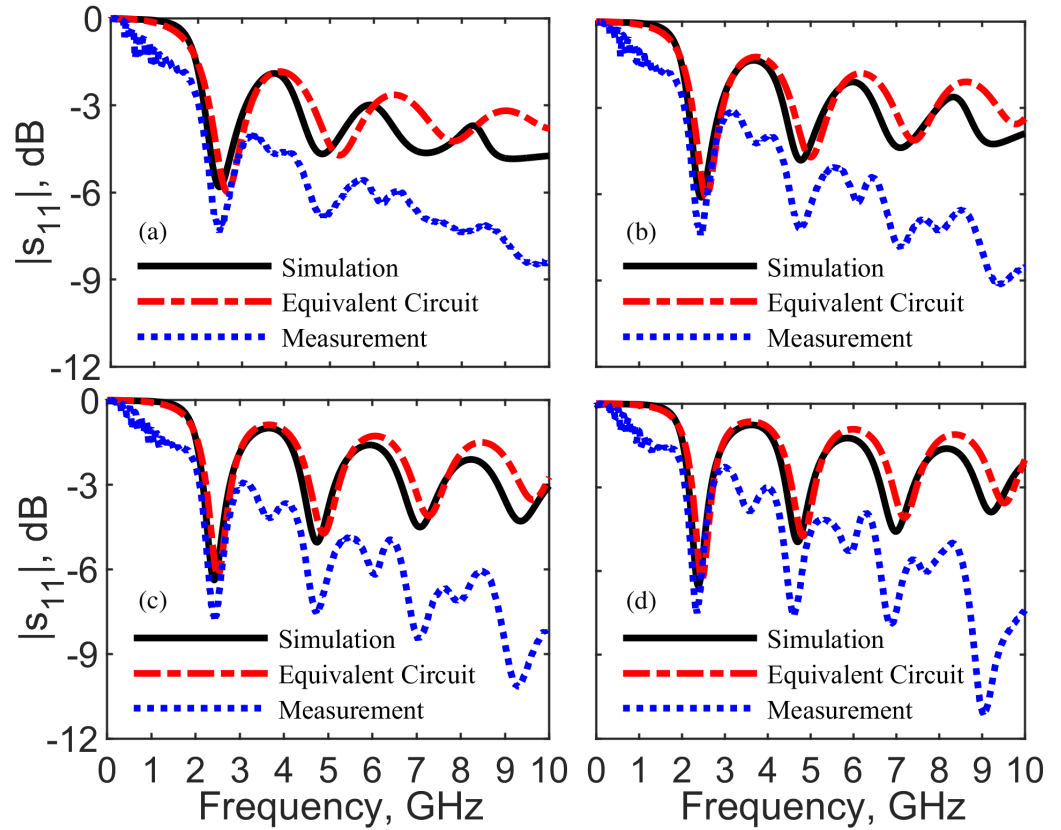


**Figure 5.** Comparison of simulations, equivalent circuit results and measurements for loops with  $U =$  (a) 8, (b) 9, (c) 10, and (d) 11.

Their values are calculated from Equations (1)–(5) [17] and are shown in Table 1. Annotations of the equations are in Table 2. The equivalent circuit models match well with the finite-element simulations at the fundamental resonance for all  $U$ s, and match better as  $U$  increases. Again, the discrepancies between measurements and the other two methods are due to the SMA adaptor. When  $U$  is lower than 9, the equivalent circuit becomes less accurate because of the non-zero reactance at the less-pronounced resonance, similar to the conclusion in [17]. The  $R$ - $L$ - $C$  pairs in the in-parallel branches for higher orders contribute to the total impedance instead of being considered as open circuits within the specific frequency range. At a larger  $U$ , such as 11, the impedance around the first resonant frequency is dominated by the first  $R_1$ - $L_1$ - $C_1$  branch, while the others can be considered almost as open circuits.

$$k_b = 2\pi b / \lambda \tag{1}$$

$$R_m \equiv m\zeta_0 \left[ \frac{k_b r_m}{m} - \frac{m}{k_b g_m} \right] \tag{2}$$

$$L_s \equiv \mu_0 b l_{um} \tag{3}$$

$$C_s \equiv \frac{\epsilon_0 b l_{\epsilon m}}{m^2} \tag{4}$$

$$Z_m = R_m + j\left(\omega L_m - \frac{1}{\omega C_m}\right) \tag{5}$$

**Table 1.** Equivalent circuit components for  $U = 8, 9, 10,$  and  $11.$

| $U$ | $R, \text{ohm}$ |         |         |         | $L, \text{nH}$ |       |        |        | $C, \text{pF}$ |        |       |       |       |       |
|-----|-----------------|---------|---------|---------|----------------|-------|--------|--------|----------------|--------|-------|-------|-------|-------|
|     | $R_0$           | $R_1$   | $R_2$   | $R_3$   | $R_4$          | $L_0$ | $L_1$  | $L_2$  | $L_3$          | $L_4$  | $C_1$ | $C_2$ | $C_3$ | $C_4$ |
| 8   |                 | 156.283 | 221.618 | 273.744 | 293.871        |       | 26.579 | 23.156 | 20.676         | 19.48  | 0.135 | 0.04  | 0.02  | 0.013 |
| 9   | 0.002           | 151.178 | 208.164 | 250.683 | 281.101        | 72.6  | 33.778 | 30.509 | 28.152         | 26.455 | 0.114 | 0.033 | 0.016 | 0.01  |
| 10  |                 | 147.551 | 201.102 | 239.225 | 270.723        |       | 40.593 | 37.29  | 34.935         | 33.11  | 0.1   | 0.028 | 0.014 | 0.008 |
| 11  |                 | 145.041 | 196.212 | 232.703 | 261.49         |       | 47.487 | 44.151 | 41.751         | 39.914 | 0.088 | 0.025 | 0.012 | 0.007 |

**Table 2.** Symbols in equations.

|       |                               |            |                                    |                  |                                |
|-------|-------------------------------|------------|------------------------------------|------------------|--------------------------------|
| $R_m$ | Modal resistance              | $g_m$      | Unitless reference value           | $k$              | Unitless variable              |
| $L_s$ | Self inductance               | $l_{um}$   | Unitless reference value           | $\epsilon_{eff}$ | Effective permittivity         |
| $C_s$ | Self capacitance              | $l_{em}$   | Unitless reference value           | $\zeta_0$        | The impedance of free space    |
| $Z_m$ | Modal impedance               | $k_b$      | Unitless reference value           | $\mu_0$          | The permeability of free space |
| $C_d$ | Total distributed capacitance | $\Omega_m$ | Lommel–Weber function of order $m$ | $\epsilon_0$     | The permittivity of free space |
| $C_t$ | Total capacitance             | $J_m$      | Bessel function of the first kind  | $a$              | The radius of a metal wire     |
| $L_m$ | Mutual inductance             | $f_1$      | Fundamental resonant frequency     | $b$              | The radius of the metal loop   |
| $r_m$ | Unitless reference value      | $m$        | The number of harmonic order       |                  |                                |

At a larger  $U$ , discrepancies are found more in higher harmonics. This is due to the fact that the equivalent circuit only considers four resonant branches, besides the zero-order one. To increase accuracies, more resonant branches need to be included in the circuit. The conclusion is that a higher  $U$  leads to a better resonance. However, the resonance performance is still not enough for resonant sensing applications, even when  $U = 11$  by which  $|s_{11}|$  is  $-6.6$  dB at the first resonance. For a fixed  $b = 20.9$  mm, the loop width  $2a$  is  $1.06$  mm for  $U = 11$ . To design a resonator with a much larger  $U$  becomes difficult as the metal width becomes too narrow for cost-effective fabrication and the loop has a high AC series resistance that increases power dissipation. For these reasons, we propose a self-tuned metal pattern for distributed impedance-matching and a better quality factor without increasing  $U$  or sacrificing the metal width.

### 3. Tuned Resonator Design

#### 3.1. Tuning Mechanism

We proposed a new impedance-matching method for a loop resonator to tune its resonance performance by embedding a metal pad, as shown in Figure 6a. The resonant frequency of the loop should stay the same, while the presence of a center pad presents a distributed capacitance  $C_d$ , by the gap between two metal patterns [18], and a mutual inductance  $L_m$ , across the gap owing to coupling magnetic fields [19].

$$C_d = \frac{2\pi b \epsilon_{eff}}{2(K(k)/(K'(k))}, \quad k = d/(d + 2a) \tag{6}$$

$$C_t = C_s + C_d \tag{7}$$

$$L_t = L_s + L_m = \frac{1}{C_t(2\pi f_1)^2} \tag{8}$$

$$r_m = \begin{cases} \frac{\pi}{8} \int_0^{2k_b} (J_{2(m+1)}(x) + J_{2(m-1)}(x)) dx & m > 0 \\ \frac{\pi}{2} \int_0^{2k_b} J_2(x) dx & m = 0 \end{cases} \tag{9}$$

$$g_m = \begin{cases} 1 / \left[ \frac{\pi}{4} \int_0^{2k_b} J_{2m}(x) dx \right] & m = 0 \\ \infty & m > 0 \end{cases} \tag{10}$$

$$l_{um} = \begin{cases} \frac{1}{2} \ln\left(\frac{8b}{a}\right) = \frac{1}{2} \sum_{k=0}^m \frac{1}{2k+1} - \frac{1}{2} \sum_{k=0}^{m-2} \frac{1}{2k+1} - \frac{\pi}{8} \int_0^{2k_b} [\Omega_{2(m+1)}(x) + \Omega_{2(m-1)}(x)] dx & m > 0 \\ \ln\left(\frac{8b}{a}\right) - 2 - \frac{\pi}{2} \int_0^{2k_b} [\Omega_2(x)] dx & m = 0 \end{cases} \quad (11)$$

$$l_{em} = \begin{cases} 2 / (\ln\left(\frac{8b}{a}\right) - 2 \sum_{k=0}^{m-1} \frac{1}{2k+1} - \frac{\pi}{2} \int_0^{2k_b} [\Omega_{2m}(x)] dx) & m > 0 \\ \infty & m = 0 \end{cases} \quad (12)$$

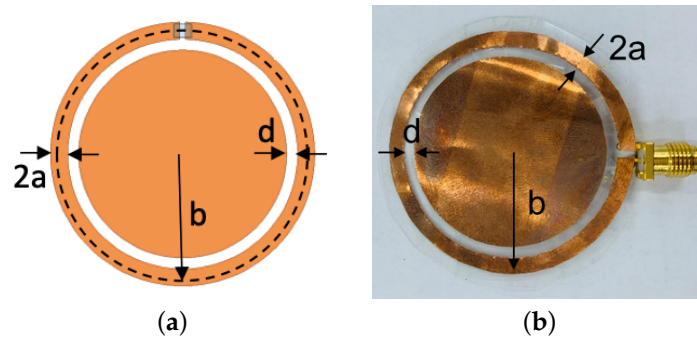


**Figure 6.** (a) Loop resonator with a center pad. *b*: Loop radius. *2a*: Loop width. *d* is the spacing distance between the metal pad and loop. (b) A photo of the tuned loop with  $U = 9$ ,  $b = 20.9$  mm,  $a = 1.44$  mm, and  $d = 1.9$  mm.

The distance between the loop and center pad *d* can serve to tune the distributed capacitances and mutual inductances presented to the loop in order to match the port impedance at the desired resonant frequency. We consider a loop with a lower value of  $U = 9$  for demonstrating the tuning effect, by which  $b = 20.9$  mm and  $a = 1.44$  mm that is not too narrow to fabricate. The gap *d* is considered between 0.1 and 8 mm.

The total capacitance  $C_t$  at the resonance can be evaluated as the capacitance  $C_s$  of the loop itself in parallel to the added distributed capacitance with a total of  $C_d$  from the length of  $2\pi b$ . The currents in the loop create magnetic fields in the gap that induces currents flowing in the opposite direction in the metal pad. From the equivalent circuit point of view, treating the loop and pad as two inductors, it appears to be a negative mutual inductance  $L_m$  that reduces the total inductance  $L_t$  presented to the port.

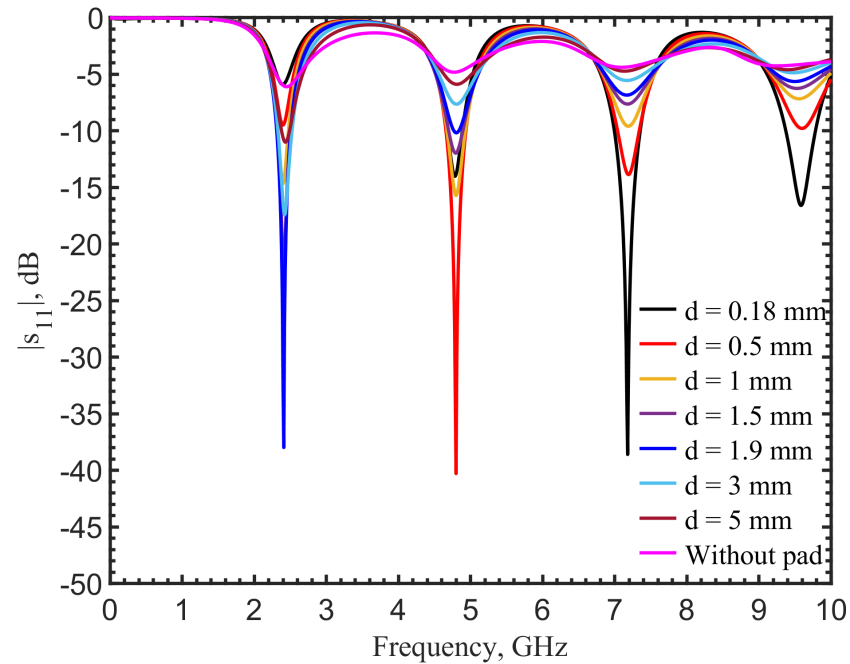
Combining the analytical formula derived by McKinley et al. [17], Equations (2), (7) and (8) give the equivalent circuit component values, while Equations (3)–(6), (9)–(12) provide the individual values for Equations (2), (7) and (8). Table 2 lists the symbol definitions. The resistance  $R_m$ , capacitance  $C_s$  and inductance  $L_s$  of the loop can be found for the equivalent resonant circuit from the impedances in Equation (5) near the resonance [17]. The values depend on *m* for the *m*th resonance. The distributed capacitance can be approximated from the two planar parallel finite-width metal-plate waveguide model [18]. Although the additional capacitance is distributed along the  $2\pi b$  circumference, we approximate the equivalent circuit value as  $C_d$ , the total distributed capacitance. Total distributed inductance  $L_t$  can be evaluated by Equation (8) as it is directly related to the fundamental resonant frequency  $f_1$ , which can be found from the formula when there is no tuning pad.  $L_m$  then can be obtained.

Table 3 lists the values of  $C_d$ ,  $L_m$ ,  $C_t$ , and  $L_t$  for each *d* between 0.5 and 5 mm for the first resonance. Increasing *d* reduces the magnitudes of  $C_d$  and  $L_m$  as the coupling becomes weaker, in return increases  $L_t$  and decreases  $C_t$ . This approach, however, could not estimate  $C_d$  or  $L_m$  at higher orders of resonance because the current distributions on the loop and the induced currents on the pad become more complicated. The parallel plate capacitance in [18] could not work for higher orders.

**Table 3.** Comparison of total distributed reactance.

| $d$ ,<br>mm | $C_d$ ,<br>pF | $L_m$ ,<br>nH | $C_t$ ,<br>pF | $L_t$ ,<br>nH | $C_{Tline}$ ,<br>pF | $L_{Tline}$ ,<br>nH |
|-------------|---------------|---------------|---------------|---------------|---------------------|---------------------|
| 0.5         | 0.133         | 16.742        | 0.248         | 17.037        | 0.216               | 20.772              |
| 1           | 0.107         | 14.683        | 0.221         | 19.095        | 0.191               | 23.178              |
| 1.5         | 0.092         | 13.303        | 0.206         | 20.475        | 0.179               | 24.31               |
| 1.9         | 0.083         | 12.422        | 0.198         | 21.356        | 0.171               | 25.53               |
| 3           | 0.067         | 10.579        | 0.182         | 23.199        | 0.164               | 26.15               |
| 5           | 0.051         | 8.203         | 0.165         | 25.576        | 0.159               | 26.28               |

Figure 7 shows the reflection coefficients for  $d = 0.18, 0.5, 1, 1.5, 1.9, 3,$  and  $5$  mm by finite-element simulations for the case of  $U = 9$  and  $b = 20.9$  mm. It is clear that the center pad improves resonance at the first four resonances, particularly the first three, without shifting their resonant frequencies. Quality factors of resonance are obtained as  $Q = f_i / \Delta f_i$ , where  $f_i$  is the  $i$ th resonant frequency and  $\Delta f_i$  is the corresponding 3-dB bandwidth. The quality factor for the first three resonant frequencies as a function of tuning distance  $d$  is shown in Figure 8. For the first resonance, a maximum quality factor of 120.5 is obtained at  $d = 1.9$  mm. To compare, the quality factor without the pad is 4.9. For the second and third resonances, the maximum quality factors are 119.6 and 119.5 when  $d = 0.5$  and  $0.2$  mm, respectively. Their counterparts without the pad are 5.3 and 4.38.

**Figure 7.** Comparison of simulations for tuned-loop resonators with different  $d$ .

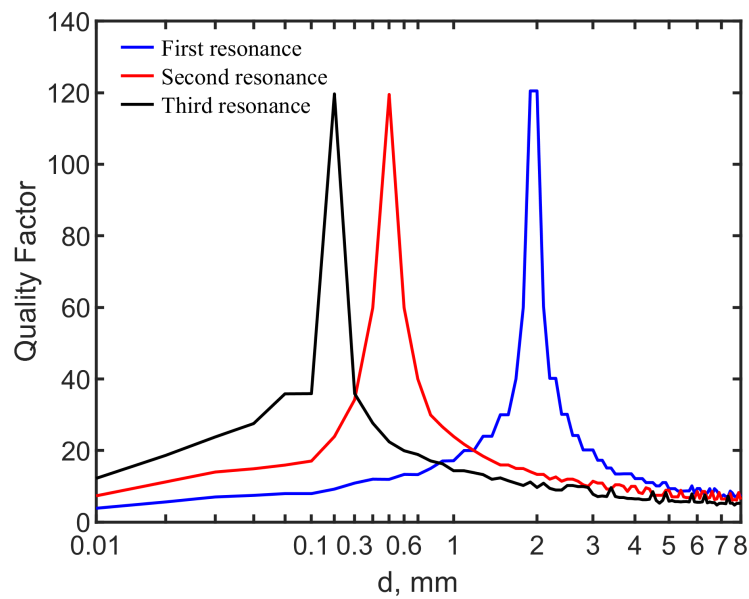


**Figure 8.** Quality factor as a function of spacing distance between the metal pad and loop  $d$ . Quality factor reaches the maximum of 120.5 for the first resonance when  $d = 1.9$ . mm. For second and third resonances, the maximum quality factors are 119.6 and 119.5 when  $d = 0.5$  and  $0.2$  mm, respectively.

### 3.2. Finite-Element Simulations

The Smith chart in Figure 9 shows how the reflection coefficients change for different  $d$  from DC to 4 GHz, compared with the one without a center pad (black curve). Although the port drives a voltage across two ends of the loop, the coupling between the loop and center pad induces current distributions on the center pad, making it similar to a virtual ground. Thus, we can look at the loop and pad from the port as a two-conductor transmission line.

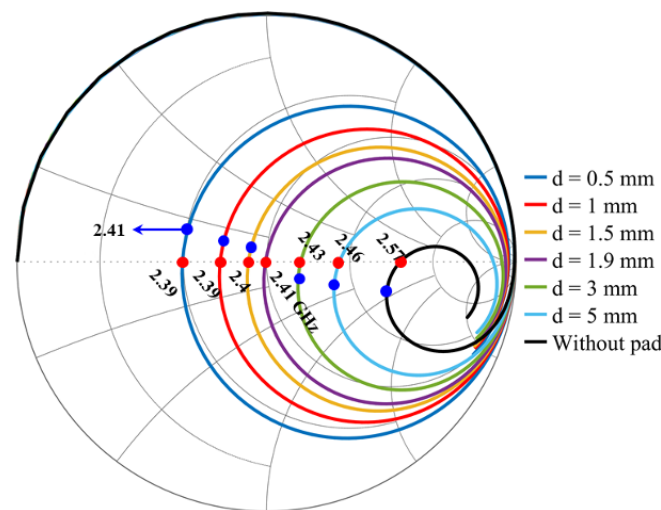


**Figure 9.** Reflection coefficient in the Smith chart among different  $d$  from DC to 4 GHz within which they cover the first resonance. When  $d = 1.9$  mm, the loop impedance is matched at the desired resonant frequency of 2.41 GHz.

The curve shapes in the Smith chart reveal that, effectively, the distributed capacitance and inductance serve to tune the characteristic impedance of such a transmission line. Thus, the self-tuned structure can be modeled as a transmission line between its first and second anti-resonant frequencies and between which the first resonance passes the zero-reactance point at the designed resonant frequency. The definition of anti-resonance is given in [15,17].

Achieving the proper  $C_d$  and  $L_m$  by a specific gap  $d$ , the impedance on the black curve from 1.09 to 3.37 GHz can be tuned to those on any curve shown in Figure 9. With  $d = 1.9$ , the impedance at 2.41 GHz is tuned close to  $50 \Omega$ . The labels in the figure show how the desired resonance frequency of 2.41 GHz varies on the Smith chart with different values of  $d$ .

The total distributed capacitance  $C_{Tline}$  and inductance  $L_{Tline}$  along the 131.3 mm circumference of the loop can be extracted from the finite-element simulation results and are listed in Table 3. The characteristic impedance can be calculated as  $\sqrt{(L_{Tline}/C_{Tline})}$ . In the case of  $d = 1.9$  mm, the return loss is significantly improved to  $-37.97$  dB from  $-6.11$  dB. The transmission-line impedance is  $386.4 \Omega$  between the first and second anti-resonant frequencies 1.09 and 3.37 GHz, respectively. For a higher order of resonance, the same method can be used to find the corresponding  $C_{Tline}$ ,  $L_{Tline}$ , and characteristic impedance for a specific frequency range. For example, the highest quality factor for the second resonant frequency of 4.79 GHz is 119.6 at  $d = 0.5$  mm. The transmission-line impedance is  $563.3 \Omega$  between 3.37 and 5.72 GHz, the second and third anti-resonant frequencies.

### 3.3. Equivalent Circuits

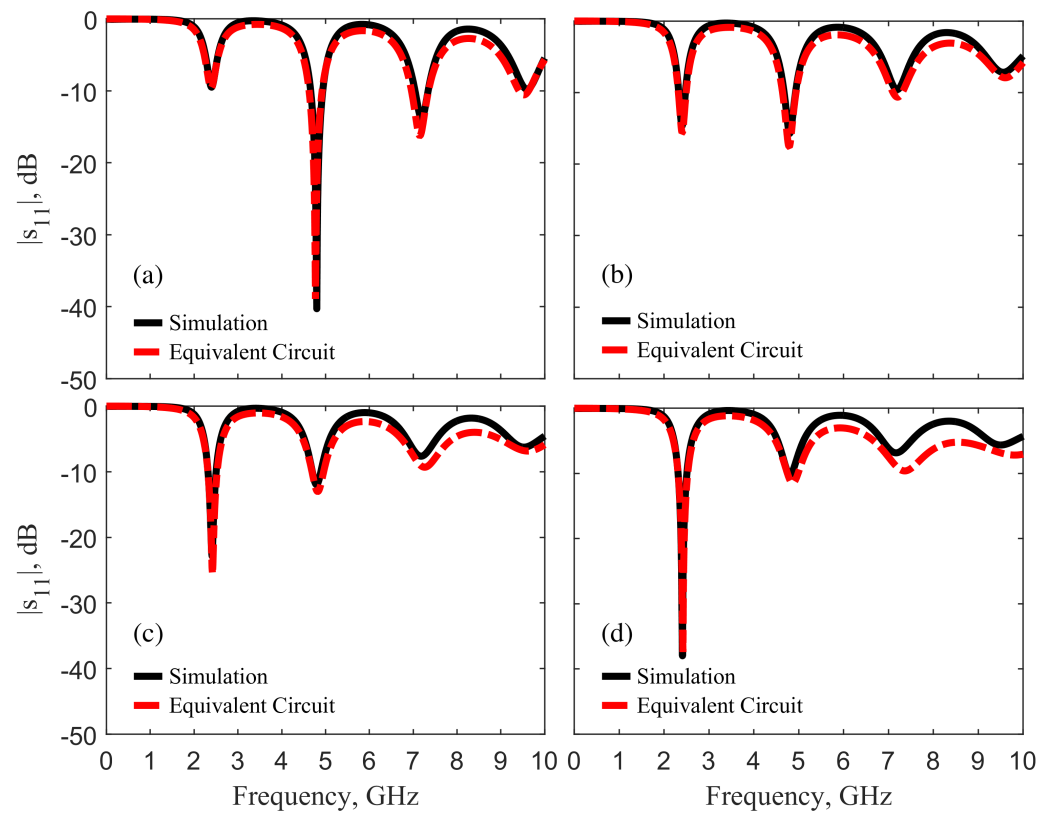
Inspired by McKinley’s equivalent circuit for the loop, in which each resonance is represented by a branch of resistor, inductor, and capacitor (RLC) components in series while orders of resonance are in parallel, we established a similar equivalent circuit for the self-tuned loop resonator. The component values were extracted from the transmission-line models for all orders of resonance in the frequency range up to 10 GHz. Five branches were considered since there were four resonances within 10 GHz. Table 4 lists the component values.

**Table 4.** Equivalent circuit components for  $d = 0.5, 1, 1.5,$  and  $1.9$  mm.

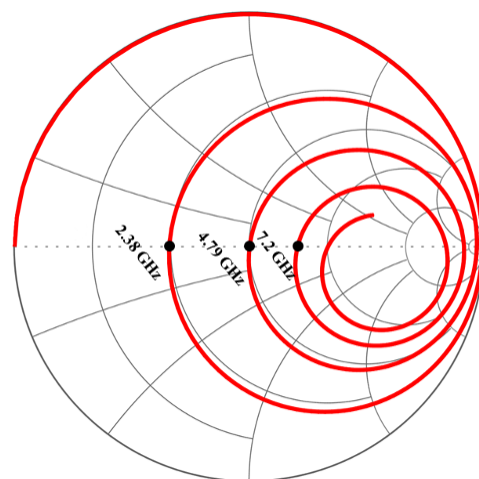
| $d, \text{ mm}$ | $R, \text{ ohm}$ |        |        |        |         | $L, \text{ nH}$ |        |        |        |        | $C, \text{ pF}$ |       |       |       |
|-----------------|------------------|--------|--------|--------|---------|-----------------|--------|--------|--------|--------|-----------------|-------|-------|-------|
|                 | $R_0$            | $R_1$  | $R_2$  | $R_3$  | $R_4$   | $L_0$           | $L_1$  | $L_2$  | $L_3$  | $L_4$  | $C_1$           | $C_2$ | $C_3$ | $C_4$ |
| 0.5             |                  | 25.125 | 49.81  | 71.13  | 91.345  |                 | 20.772 | 18.791 | 15.768 | 12.602 | 0.216           | 0.059 | 0.031 | 0.022 |
| 1               | 0.002            | 35.88  | 67.25  | 97.86  | 120.13  | 72.6            | 23.178 | 20.142 | 15.831 | 13.595 | 0.191           | 0.055 | 0.031 | 0.02  |
| 1.5             |                  | 45.22  | 82.565 | 114.39 | 141.565 |                 | 24.31  | 20.243 | 15.166 | 11.46  | 0.179           | 0.054 | 0.032 | 0.023 |
| 1.9             |                  | 49.48  | 92.635 | 117.84 | 137.86  |                 | 25.53  | 19.092 | 12.795 | 8.016  | 0.171           | 0.056 | 0.037 | 0.032 |

Figure 10 shows the comparison between the results from the equivalent circuits and finite-element simulations, with good agreement, for  $d = 0.5, 1, 1.5,$  and  $1.9$  mm. It is expected that more discrepancies occur at the third and fourth resonances because the equivalent circuits only include four resonant branches. More branches can increase accuracy. However, the transmission line model may not work well at higher modes of resonance because the current distributions on the loop and pad start to mix with more harmonics.

It is noted that  $d = 1.9$  mm clearly improves the first resonance while  $d = 0.5$  mm improves the second resonance significantly. This can be observed from the Smith chart shown in Figure 11, in which the second resonant point at 4.79 GHz for  $d = 0.5$  mm reaches good impedance-matching to  $50 \Omega$ , while the real part of the impedance is  $24.78 \Omega$  at the first resonant frequency of 2.39 GHz. Compared to the Smith chart in Figure 9, at 2.41 GHz, the real part of impedance for  $d = 1.9$  mm becomes  $49.73 \Omega$  when the reactance becomes zero.



**Figure 10.** Comparison of simulations and equivalent circuit results in different  $d =$  (a) 0.5, (b) 1, (c) 1.5, (d) 1.9 mm.



**Figure 11.** Reflection coefficient in the Smith chart for  $d = 0.5$  mm from DC to 10 GHz within which it covers the first four orders of resonance.  $s_{11}$  passes through the matching point at the 2nd resonant frequency of 4.79 GHz.

Figure 12 compares the impedances from the equivalent circuits of the loop being untuned (red curves) and tuned (blue) with  $d = 1.9$  mm. The untuned curves match well with the results in [17]. Two sets of resonance and anti-resonance points are illustrated in the figure. In the resonance point, reactance changes from capacitive to inductive while the real part of impedance reaches a local minimum. At the anti-resonance point, although the reactance crosses zero from inductive to capacitive, the resistance reaches the local maximum, indicating little current flowing. The reactance amplitude variations indicate how pronounced the resonance between them is. In this comparison, the resistance of the

tuned loop (blue, solid curve) with  $d = 1.9$  mm is  $49.73 \Omega$  at the first resonance point, while the resistance for the untuned one (red, dashed) is  $145.8 \Omega$ .

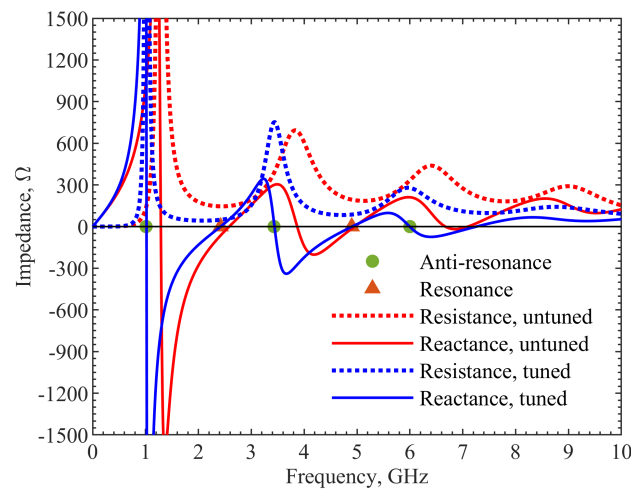


**Figure 12.** Comparison of impedances from the equivalent circuits of loop resonators of  $U = 9$  tuned and untuned. The first three anti-resonance and two resonance points are labeled for the tuned loop resonator where the reactance become zero (blue, solid curve). The real part of the impedance (blue, dotted curve) distinguishes resonance from anti-resonance.

For the first resonance frequency, the total distributed capacitance and inductance of the loop circumference calculated by Equations (7) and (8) are compared with the values from the transmission-line model, shown in Figure 13. The discrepancy is noticeable when  $d$  is smaller. This is because the field distribution assumption deviates from the one in the two in-parallel metal plates with finite widths in [18]. As the field strength becomes higher between the smaller gap, the edge effects on the far edge in one plate are more pronounced as compared to our case in which the center pad has no far edge. The edge effect is not considered in the formula. Additionally, the elliptic integral diverges  $K'(k)$  logarithmically as  $1/k$  when the variable  $k$  is smaller than 0.4 in Equation (6). The similar discrepancy has also been discussed in [18]. In our cases,  $k$  is 0.15, 0.26, 0.34, 0.4, 0.51 and 0.63 for  $d = 0.5, 1, 1.5, 1.9, 3$  and  $5$  mm, respectively. Therefore, discrepancies between the transmission-line model and analytical values are expected when the spacing  $d$  becomes smaller.

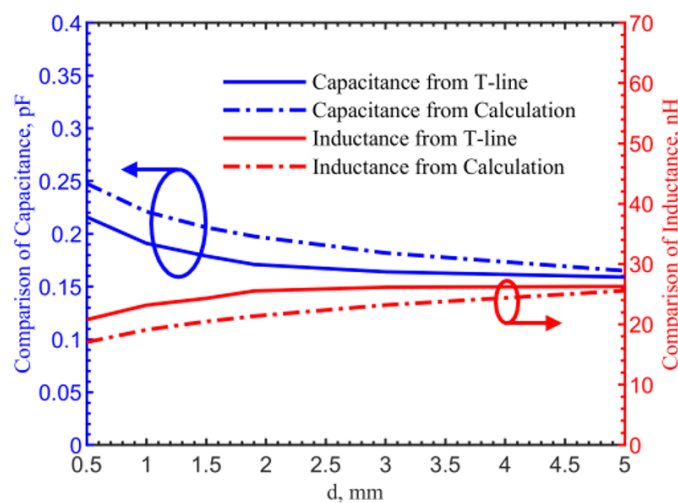


**Figure 13.** Comparison of the theoretical and transmission-line model values for the capacitance and inductance of the tuned loop.

It is clear that the self-tuned configuration can significantly improve the resonance of a loop resonator at the desired resonant frequency. The performance can be predicted with the equivalent circuits with sufficient accuracy.

## 4. Experimental Results

### 4.1. Results of The Self-Tuned Loop Resonator with $U = 9$

A loop resonator with  $U = 9$ , which has  $b = 20.9$  mm and  $2a = 2.88$  mm, made of a thin copper sheet, is chosen for demonstration. The fundamental resonant frequency is designed at 2.41 GHz. In the case of the tuned loop, the center pad is fixed with three small pieces of thin transparent tape. The rings are not supported by any substrate to avoid any effect from the substrate to the loop performance in order to validate the theories in [15,17]. The radius of the center pad is 17.56 mm, and the tuning gap  $d$  is 1.9 mm, as shown in Figure 6b.

The device is connected to a vector network analyzer (Keysight PNA N5227B) via an SMA adaptor. The s-parameters are extracted at 801 frequency sampling points from 100 MHz to 10 GHz. Figure 14 shows the comparison of reflection coefficients of the loop resonators with and without the center pad. The measurements match well with the simulations indicating significant improvement in resonance with the tuning structure. At the fundamental resonance, the reflection coefficient is expected to improve from  $-6.11$  to  $-37.97$  dB, while the measurements show an improvement from  $-7$  to  $-29.5$  dB. At the second resonance, the measured  $|s_{11}|$  is improved from  $-7.2$  dB to  $-17.25$  dB, compared to the theoretical improvement from  $-4.82$  dB to  $-10.17$  dB. The discrepancies between simulations and measurements are mainly due to the SMA adaptor, which will be validated in the Section 5.

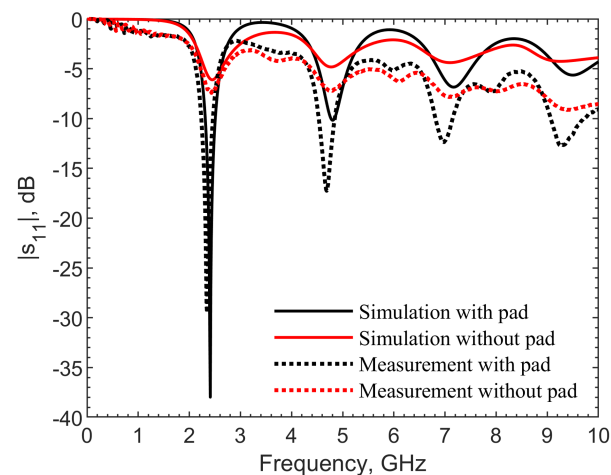


**Figure 14.** Comparison of measurements and simulations for tuned ( $d = 1.9$  mm) and untuned loop resonators, both with  $U = 9$ .

### 4.2. Optimal $d$ for $U$

For a simple loop,  $U$  needs to be larger than 9 to have a decent resonance performance. Figures 3 and 4 show the theoretical and measured quality factors for the first resonant frequency are only 9.154 and 6.438, even for  $U = 11$ . The spectral curves indicate the performance for the loops with  $U = 8$  and 9 degrades at higher orders of resonance. Attempts to increase  $U$  further, however, make the metal pattern too narrow.

We examine loops with the same radius  $b$  but different  $U$  from 8 to 11. The optimal tuning gap  $d$  for each  $U$  is found in the same way shown in Figure 9, targeting the maximum quality factor at the first resonant frequency. The  $d$ s are 1.1, 2.5, and 2.77 mm for  $U = 8$ , 10, and 11, respectively. Figure 15 shows the results. The tuning center pad dramatically improves the resonance performance for  $U = 8, 9, 10, 11$ , with  $|s_{11}|$  from  $-5.8, -6.11, -6.38, -6.53$  dB at 2.49, 2.45, 2.42, and 2.38 GHz, to  $-38.65, -37.97, -39.82, -40.12$  dB at 2.50,

2.41, 2.37, and 2.35 GHz, respectively. The quality factors are improved from 3.44, 4.9, 7.56, and 9.15, to 62.5, 120.5, 118.5, and 117.5, for  $U = 8, 9, 10, 11$ , respectively.

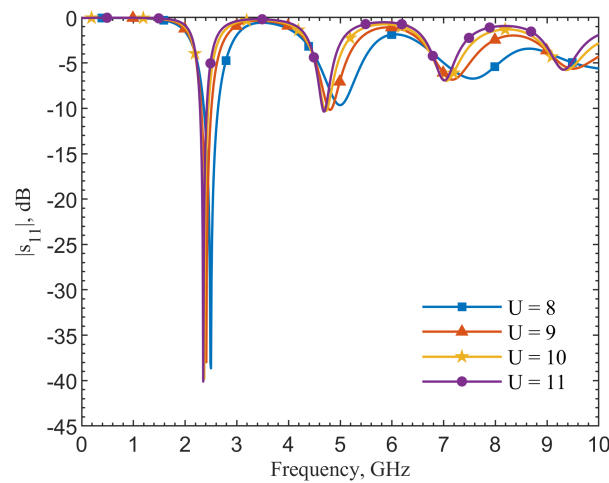


**Figure 15.** Comparison of tuned-loop resonators with  $U$  from 8 to 11.

As discussed earlier, a larger  $U$  leads to a better resonance when there is no tuning pad. However, with an optimum tuning gap designed for the first resonant frequency, the quality factors between  $U = 9$  and 11 are similar and higher than  $U = 8$ . For a small  $U$ , which holds the benefit of having a wider metal loop width, the quality factor can be tuned to be similar to that of a larger  $U$ . Furthermore, the tuning also allows the gap distance to be optimized at a higher order of resonance.

## 5. Discussion

### 5.1. Discrepancy Investigation

The measurements in Sections 2 and 4 match well with their respective simulations. However, one notices the measurement result has higher losses as frequency increases and dips in the spectral shapes, especially around the anti-resonance points where  $|s_{11}|$  has local peaks. These effects are mainly due to the SMA adaptor between the planar loop and coaxial cable. In comparison, simulations were conducted by placing a  $50\text{-}\Omega$  excitation port directly across the ends of the loop.

A 3-D SMA adaptor model was built in the finite-element tool with the exact dimensions of the adaptor. The materials were specified as Teflon and copper. Simulations were conducted for the loop resonator of  $U = 9$ , with and without the center pad. The results are compared with measurement in Figure 16. As it can be seen, the overall slopes of additional insertion losses appear in the simulations, and their overall spectral trends now match with those from measurements. The curves for tuned and untuned loops match well at the first resonance. Above 3 GHz, the resonant frequencies at higher orders have more discrepancies. The losses become less for the measured result at resonances above 5 GHz compared to simulations. This is possibly due to the fact the materials used in the 3-D SMA model may not have the exact frequency-dependent characteristics of the materials used in the physical adaptor. For the loop resonator without a tuning pad, in the red color, both curves show unpronounced third and fourth resonances, while measurements match simulations at the first and second resonances well. Thus, it is clear that the discrepancies above 3 GHz in measurements come from the SMA adaptor. Such an issue will not exist if the resonator is designed with monolithic electronics integration. Even with the effect of an imperfect adaptor, all four resonances in the tuned loop, shown by the black dashed curve, are more pronounced and robust in measurements.

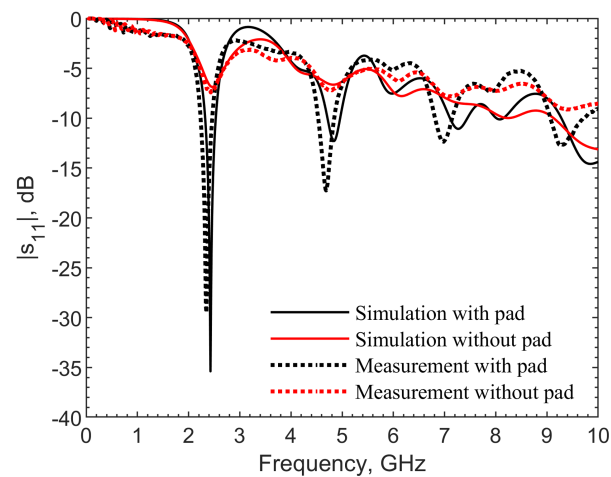


**Figure 16.** Comparison of measurements and simulations for tuned- and untuned-loop resonators with  $U = 9$ . Both have a SMA adaptor between the device and coaxial cable. The simulations are conducted with a 3-D SMA adaptor model included. The calibration is conducted at the coaxial output of the SMA adaptor. The tuned loop resonator has  $d = 1.9$  mm.

### 5.2. Effect of Substrate

The tuning method for loop resonator impedance-matching has been verified by finite-element simulations, equivalent circuits, and corresponding measurements without substrates because the original model established by Storer [15] and McKinley et al. [17] is simply a loop suspended in air, and the loop is made of a thin wire. In our work, we utilized the formula for planar loops with limited metal width. In order to limit variables, we used thin tapes to fix the loop and the metal pad, so the substrate effects did not appear.

In practical scenarios, substrates are needed to support the resonator. The substrate added a fixed value to the effective dielectric constant, and a thick dielectric layer or a high substrate dielectric constant may add substrate modes that affect the impedances. For lower substrate dielectric constants, the resonant frequency of the loop resonator will still shift, responding to the changes in the overall effective permittivity. To investigate the effects, finite-element simulations were conducted on a loop resonator with the substrate of various dielectric constants. The dimensions of the loop were the same as those in Sections 2 and 4, with  $b = 20.9$  mm and  $2a = 2.88$  mm ( $U = 9$ ). Figure 17 shows the results of resonant frequencies as a function of substrate dielectric constant from 1 to 8 for a substrate thickness of 1.5 mm. The resonant frequency monotonically reduced to 1.67 GHz when the dielectric constant increased to 8, as expected.

To experimentally test the tuning performance, a one-layer FR4 board (uxcell, China) with a thickness of 1.5 mm and a dielectric constant of 4.4 was used as the substrate. The copper thickness was  $34.5$   $\mu\text{m}$ . The optimum  $d$  is found as 4.85 mm by repeating the procedures described in Section 3. Simulations with and without a tuning pad were conducted for comparison, and the tuned resonance performance was significantly improved from  $-7.99$  dB to  $-45.47$  dB at 1.905 GHz, as expected by the tuning mechanism. In measurements, loop resonators with and without a tuning pad under the same configuration were fabricated by photolithography and copper etching, as shown in Figure 18. The measured reflection coefficients are compared with those from simulations in Figure 19. The measured  $|s_{11}|$  was improved from  $-8.23$  dB to  $-37.34$  dB at 1.89 GHz, which matched well with the simulation results. The results indicate that the tuning method is also applicable to loops on substrates to enhance resonance.

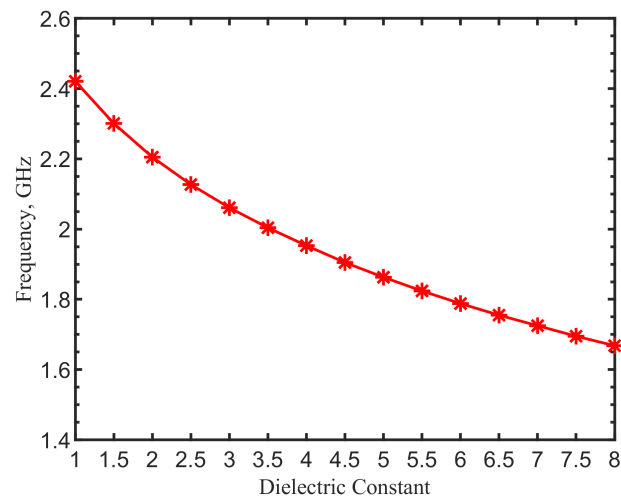


**Figure 17.** Resonant frequencies as a function of substrate dielectric constant from 1 to 8 for the loop resonator ( $U=9, b = 20.9$  mm,  $a = 1.44$  mm).

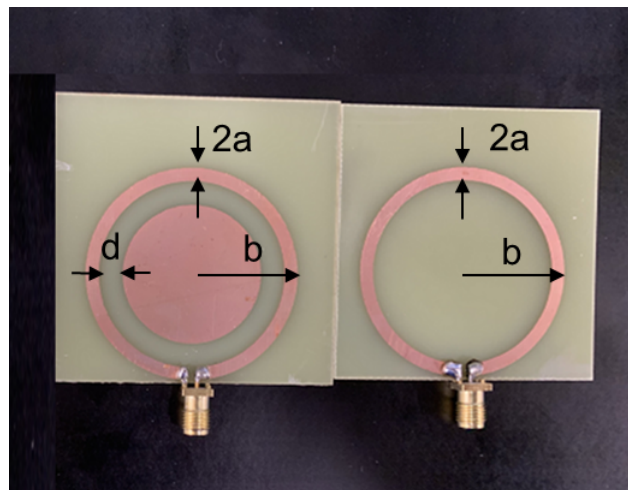


**Figure 18.** Photo of loop resonators fabricated on FR4 substrates with and without a tuning center pad.  $U=9, b = 20.9$  mm,  $a = 1.44$  mm, and  $d = 4.85$  mm.

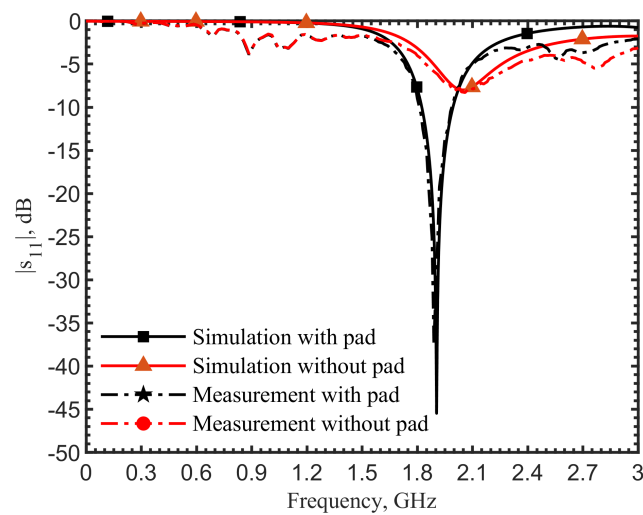


**Figure 19.** Comparison of measurements and simulations for tuned- ( $d = 4.85$  mm) and untuned-loop resonators on FR4 substrates with a 1.5 mm thickness.

## 6. Conclusions

A new tuning method for impedance-matching of loop resonators has been proposed and demonstrated in this work. By varying the spacing distances between the metal pad and loop, the reactance can be tuned to match the port impedance at the desired resonant frequency. First, with the single-wire-loop theory developed in [17], analytical equations and equivalent circuits based on the impedances at resonance were verified with measurements for the planar loop configurations. We demonstrated the tuning procedure within an ISM-band frequency band. The optimum gap spacing for a configuration with  $U = 9$ , by which a good trade-off was reached between the metal loop radius and width, was found at 1.9 mm. The theory was verified by finite-element simulations and measurements. An equivalent circuit was established for the tuned loop. High orders of resonance could also be tuned depending on the need. It was clear that the resonance performance at the desired resonant frequency could be significantly improved and more robust.

Loop resonators and similar device architectures used in meta-materials can be optimized at the desired resonant frequency by the proposed tuning method without changing their overall sizes. Robust resonance performance has been validated by experiments, even given the degrading factor contributed by SMA adaptors. The structure with robust resonance can provide great advantages for sensing or near-field signal/power coupling as the dielectric characteristics of the environments may be uncontrollable or unpredictable. For example, such a compact planar resonator with a high quality factor was recently utilized by us for enhancing wireless power coupling in a subcutaneous implant system [20,21] and improving sensitivity for a near-field water-content sensor [22]. In these systems, the designs followed the principles, analytical formula, and equivalent circuits in this work. The robust resonance ensured that the power coupling efficiency stayed sufficient when the implant depth varied, by which the effective dielectric permittivity presented to the resonator changed. The significantly improved quality factor allowed the sensitivity to tissue permittivities remain the same when the body dehydration levels changed, or water contents changed in pork patties and fruits. These applications utilizing the simple-loop resonators were enabled by the greatly improved resonance.

**Author Contributions:** Conceptualization, J.-C.C. and S.B.; methodology, J.-C.C. and S.B.; software, S.B.; validation, S.B. and K.C.; formal analysis, J.-C.C. and S.B.; resources, J.-C.C.; data curation, S.B.; writing—original draft preparation, S.B.; writing—review and editing, J.-C.C. and S.B.; visualization, S.B.; supervision, J.-C.C.; project administration, J.-C.C.; funding acquisition, J.-C.C. All authors have read and agreed to the published version of the manuscript.

**Funding:** This research was funded by National Science Foundation ENG-CMMI-1929953, and Mary and Richard Templeton endowment.

**Institutional Review Board Statement:** Not applicable.

**Informed Consent Statement:** Not applicable.

**Data Availability Statement:** The data presented in this study are available on request from the corresponding author.

**Acknowledgments:** The authors sincerely appreciate the facility and financial support from the Lyle School of Engineering and the generosity of Mary and Richard Templeton.

**Conflicts of Interest:** The authors declare no conflicts of interest.

## References

1. Pendry, J.; Holden, A.; Robbins, D.; Stewart, W. Magnetism from Conductors and Enhanced Nonlinear Phenomena. *IEEE Trans. Microw. Theory Tech.* **1999**, *47*, 2075–2084. [[CrossRef](#)]
2. Marqués, R.; Martín, F.; Sorolla, M. *Metamaterials with Negative Parameters: Theory, Design, and Microwave Applications*, 1st ed.; Wiley: Hoboken, NJ, USA, 2008; Volume 183.
3. Chowdhury, D.R.; Singh, R.; Reiten, M.; Chen, H.T.; Taylor, A.J.; O'Hara, J.F.; Azad, A.K. A Broadband Planar Terahertz Metamaterial with Nested Structure. *Opt. Express* **2011**, *19*, 15817–15823. [[CrossRef](#)]

4. Rockstuhl, C.; Zentgraf, T.; Guo, H.; Liu, N.; Etrich, C.; Loa, I.; Syassen, K.; Kuhl, J.; Lederer, F.; Giessen, H. Resonances of Split-ring Resonator Metamaterials in the Near Infrared. *Appl. Phys. B Lasers Opt.* **2006**, *84*, 219–227. [[CrossRef](#)]
5. Delgado, V.; Sydoruk, O.; Tatartschuk, E.; Marqués, R.; Freire, M.; Jelinek, L. Analytical Circuit model for Split Ring Resonators in the Far Infrared and Optical Frequency Range. *Metamaterials* **2009**, *3*, 57–62. [[CrossRef](#)]
6. Enkrich, C.; Wegener, M.; Linden, S.; Burger, S.; Zschiedrich, L.; Schmidt, F.; Zhou, J.F.; Koschny, T.; Soukoulis, C.M. Magnetic Metamaterials at Telecommunication and Visible Frequencies. *Phys. Rev. Lett.* **2005**, *95*, 203901. [[CrossRef](#)] [[PubMed](#)]
7. Locatelli, A. Peculiar Properties of Loop Nanoantennas. *IEEE Photonics J.* **2005**, *3*, 845–853. [[CrossRef](#)]
8. Aydin, K.; Bulu, I.; Guven, K.; Kafesaki, M.; Soukoulis, C.M.; Ozbay, E. Investigation of Magnetic Resonances for Different Split-ring Resonator Parameters and Designs. *New J. Phys.* **2005**, *7*, 168. [[CrossRef](#)]
9. Baghelani, M.; Abbasi, Z.; Daneshmand, M.; Light, P.E. Non-invasive Continuous-time Glucose Monitoring System Using a Chipless Printable Sensor Based on Split Ring Microwave Resonators. *Sci. Rep.* **2020**, *10*, 12980. [[CrossRef](#)] [[PubMed](#)]
10. Ekinici, G.; Calikoglu, A.; Solak, S.N.; Yalcinkaya, A.D.; Dundar, G.; Torun, H. Split-ring Resonator-based Sensors on Flexible Substrates for Glaucoma Monitoring. *Sens. Actuators A Phys.* **2020**, *268*, 32–37. [[CrossRef](#)]
11. Choi, H.; Naylor, J.; Luzio, S.; Beutler, J.; Birchall, J.; Martin, C.; Porch, A. Design and In Vitro Interference Test of Microwave Noninvasive Blood Glucose Monitoring Sensor. *IEEE Trans. Microw. Theory Tech.* **2015**, *63*, 3016–3025. [[CrossRef](#)] [[PubMed](#)]
12. Choi, H.; Luzio, S.; Beutler, J.; Porch, A. Microwave Noninvasive Blood Glucose Monitoring Sensor: Human Clinical Trial Results. In Proceedings of the 2017 IEEE MTT-S International Microwave Symposium (IMS), Honolulu, HI, USA, 4–9 June 2017; IEEE: Piscataway, NJ, USA, 2017; pp. 876–879.
13. Torun, H.; Top, F.C.; Dundar, G.; Yalcinkaya, A.D. A Split-ring Resonator-based Microwave Sensor for Biosensing. In Proceedings of the 2014 International Conference on Optical MEMS and Nanophotonics, Glasgow, UK, 17–21 August 2014; University of Strathclyde: Glasgow, UK, 2014; pp. 159–160.
14. Mueh, M.; Damm, C. Spurious Material Detection on Functionalized Thin-Film Sensors using Multiresonant Split-Rings. In Proceedings of the 2018 IEEE International Microwave Biomedical Conference (IMBioC), Philadelphia, PA, USA, 14–15 June 2018; IEEE: Piscataway, NJ, USA, 2018; pp. 196–198.
15. Storer, J.E. Impedance of Thin-wire Loop Antennas. *Trans. Am. Inst. Electr. Eng. Part 1 Commun. Electron.* **1956**, *75*, 606–619. [[CrossRef](#)]
16. Wu, T.T. Theory of the Thin Circular Loop Antenna. *J. Math. Phys.* **1962**, *3*, 1301–1304. [[CrossRef](#)]
17. McKinley, A.F.; White, T.P.; Maksymov, I.S.; Catchpole, K.R. The Analytical Basis for the Resonances and Anti-resonances of Loop Antennas and Meta-material Ring Resonators. *J. Appl. Phys.* **2012**, *112*, 94911. [[CrossRef](#)]
18. Wei, J. Distributed Capacitance of Planar Electrodes in Optic and Acoustic Surface Wave Devices. *IEEE J. Quantum Electron.* **1977**, *13*, 152–158. [[CrossRef](#)]
19. Maradei, F.; Caniggia, S. Appendix A: Formulae for Partial Inductance Calculation. In *Signal Integrity and Radiated Emission of High-Speed Digital Systems*; Francescaromana, M., Caniggia, S., Eds.; John Wiley & Sons, Ltd.: Chichester, UK, 2008; pp. 481–486.
20. Bing, S.; Chawang, K.; Chiao, J.C. Resonant Coupler Designs for Subcutaneous Implants. In Proceedings of the 2021 IEEE Wireless Power Transfer Conference (WPTC), San Diego, CA, USA, 1–4 June 2021; IEEE: Piscataway, NJ, USA, 2021; pp. 1–4.
21. Bing, S.; Chawang, K.; Chiao, J.C. A Resonant Coupler for Subcutaneous Implant. *Sensors* **2021**, *21*, 8141. [[CrossRef](#)] [[PubMed](#)]
22. Bing, S.; Chawang, K.; Chiao, J.C. A Radio-Frequency Planar Resonant Loop for Noninvasive Monitoring of Water Content. In Proceedings of the 2022 IEEE Sensors, Dallas, TX, USA, 30 October–2 November 2022; IEEE: Piscataway, NJ, USA, 2022; pp. 1–4.